CATALYSIS

Dynamic multinuclear sites formed by mobilized copper ions in NO_x selective catalytic reduction

Christopher Paolucci,[1] Ishant Khurana,[2] Atish A. Parekh,[2] Sichi Li,[1] Arthur J. Shih,[2] Hui Li,[1] John R. Di Iorio,[2] Jonatan D. Albarracin-Caballero,[2] Aleksey Yezerets,[3] Jeffrey T. Miller,[2] W. Nicholas Delgass,[2] Fabio H. Ribeiro,[2] William F. Schneider,[1]* Rajamani Gounder[2]*

Copper ions exchanged into zeolites are active for the selective catalytic reduction (SCR) of nitrogen oxides (NO_x) with ammonia (NH_3), but the low-temperature rate dependence on copper (Cu) volumetric density is inconsistent with reaction at single sites. We combine steady-state and transient kinetic measurements, x-ray absorption spectroscopy, and first-principles calculations to demonstrate that under reaction conditions, mobilized Cu ions can travel through zeolite windows and form transient ion pairs that participate in an oxygen (O_2)–mediated $Cu^I \rightarrow Cu^{II}$ redox step integral to SCR. Electrostatic tethering to framework aluminum centers limits the volume that each ion can explore and thus its capacity to form an ion pair. The dynamic, reversible formation of multinuclear sites from mobilized single atoms represents a distinct phenomenon that falls outside the conventional boundaries of a heterogeneous or homogeneous catalyst.

Single-site heterogeneous catalysts promise to combine the attractive features of homogeneous and heterogeneous catalysts: active sites of regular and tunable architecture that provide precise catalytic function, integrated into a thermally stable, porous, solid host that facilitates access of substrates to those sites and separation of products from the catalyst (*1*). In the conventional definition, a single-site catalyst contains functionally isolated active sites, such that reaction rates per active site are independent of their spatial proximity (*2*). Single metal atoms incorporated into solid oxide supports are reported to follow this conventional single-site behavior in catalytic CO oxidation to CO_2 (*3*–*5*), selective hydrogenation (*6*, *7*), and water-gas shift (*8*, *9*). Here we report that a nominally single-site catalyst (*10*) operates by dynamic, reversible, and density-dependent (non–mean field) interaction of multiple ionically tethered single sites, a behavior that lies outside the canonical definition of a single-site heterogeneous catalyst (*11*).

We discovered this phenomenon in the quest for a molecularly detailed model to unify the seemingly disparate observations of the catalytic function of copper-exchanged chabazite (Cu-CHA) zeolites, materials used in emissions control for the standard selective catalytic reduction (SCR) of nitrogen oxides (NO_x, x = 1, 2) with ammonia (*12*)

$$4NO + O_2 + 4NH_3 \rightarrow 4N_2 + 6H_2O \quad (1)$$

Chabazite is a small-pore zeolite composed of cages (8 Å by 8 Å by 12 Å) interconnected by six-membered ring (6-MR) prisms and eight-membered ring (8-MR) windows (Fig. 1A). Substitution of Si^{4+} by Al^{3+} within the framework introduces an anionic charge that is balanced by extra-lattice cations. After Cu ion exchange and high-temperature oxidation treatment, two isolated Cu site motifs are present: discrete Cu^{II} ions that balance two proximal Al centers and $[Cu^{II}OH]^+$ ions that balance single Al centers (*10*, *13*, *14*). Under low-temperature (<523 K) standard SCR conditions, ammonia coordinates to and liberates Cu ions from direct association with the zeolite support, and these solvated Cu ions act as the redox-active catalytic sites (*15*). At typical Cu ion volumetric densities, standard SCR rates increase linearly with Cu density, as expected for a single-site catalyst. As shown here, however, experimental observations in the low–Cu density limit reveal a portion of the catalytic cycle in which O_2 activation by transiently formed Cu pairs becomes rate limiting. These Cu pairs form from NH_3-solvated Cu ions with mobilities restricted by electrostatic attraction to charge-compensating framework Al centers, leading to catalytic function that is neither single site nor homogeneous.

Recognizing the intermediacy of this distinct catalytic state reconciles a number of controversies in Cu-zeolite SCR catalysis, including the role of the zeolite support in the catalytic mechanism, the sensitivity of SCR rates to Cu density under different conditions of observation, the extent to which standard and the closely related fast SCR cycles (*16*) are connected through common intermediates, the chemical processes that limit low-temperature NO_x SCR reactivity, and the origins of the apparent change in mechanism at elevated temperatures. These observations provide insight into the design of improved catalysts for SCR. More broadly, they reveal a distinct class of catalytic materials characterized by partially mobile ions that dynamically and reversibly form multinuclear active sites, a concept that may be exploited for a wide variety of reactions.

Turnover rates depend on the spatial density of single Cu sites

To assess the catalytic consequences of Cu ion density, we prepared a series of Cu-CHA samples with fixed framework Al composition (Si/Al = 15) and Cu/Al content ranging from 0.04 to 0.44 [for synthesis methods and characterization data, see supplementary materials (SM) section S1, figs. S1 to S4, and tables S1 and S2], corresponding to Cu volumetric densities (ρ_{Cu}) from (0.3 to 4.2) × 10^{-4} Cu $Å^{-3}$. We denote samples as Cu-CHA-X, where X indicates the mean Cu-Cu distance (in Å), assuming a homogeneous Cu distribution (table S2). Mean Cu-Cu distances vary from 40.7 to 16.6 Å from the least to most heavily Cu-exchanged samples, and the highest Cu loading corresponds to approximately one Cu ion per three chabazite cages (Fig. 1A).

We observed that SCR rates increased linearly with Cu density at $\rho_{Cu} > 1.9 \times 10^{-4}$ $Å^{-3}$ (Fig. 1B), as would be expected for a reaction catalyzed by isolated Cu sites. Turnover rates, apparent reaction orders, and apparent activation energies (table S3) are consistent with values reported for high–Cu density Cu-CHA samples (*17*, *18*). By contrast, standard SCR rates vary quadratically with Cu density below $\rho_{Cu} < 1.13 \times 10^{-4}$ $Å^{-3}$. All kinetic quantities are consistent with those reported for Cu-dilute Cu-CHA samples [Si/Al = 4.5, Cu/Al < 0.02 (*17*); Si/Al = 6, Cu/Al < 0.03 (*18*)]. We show that these two kinetic regimes, characterized by distinct kinetic parameters, reflect different rate-controlling elementary steps and prevalent reactive intermediates during steady-state NO_x SCR.

To probe the mechanistic origins of this change in kinetic behavior, we used x-ray absorption near-edge structure (XANES) spectroscopy to quantify Cu oxidation state during steady-state standard SCR in operando. Figure 2 and table S4 report the steady-state Cu^I fraction obtained by XANES fitting (procedure detailed in SM section S3) as a function of Cu density for three samples in Fig. 1 (Si/Al = 15) and seven other Cu-CHA zeolites (Si/Al = 4.5, 16, and 25; table S4). Consistent with prior observation, the site-isolated Cu^{II} ions observed ex situ evolve into a mixture of Cu^I and Cu^{II} ions during standard SCR catalysis, indicative of redox cycling between Cu^I and Cu^{II} oxidation states coupled with the SCR catalytic cycle (*12*). The $Cu^{II} \rightarrow Cu^I$ half-cycle (Fig. 2, inset) is accepted to occur on site-isolated Cu^{II}, to consume one equivalent of NO and NH_3 per Cu^{II}, and to produce N_2 and H_2O (*15*, *16*).

The inverse relationship between steady-state Cu^I fraction and Cu volumetric density (Fig. 2) is inconsistent with the behavior expected of a single-site catalyst, for which the active-site oxidation state should depend only on the reaction

[1]Department of Chemical and Biomolecular Engineering, University of Notre Dame, Notre Dame, IN 46556, USA. [2]Charles D. Davidson School of Chemical Engineering, Purdue University, 480 Stadium Mall Drive, West Lafayette, IN 47907, USA. [3]Cummins Inc., 1900 McKinley Avenue, MC 50183, Columbus, IN 47201, USA.
*Corresponding author. Email: wschneider@nd.edu (W.F.S.); rgounder@purdue.edu (R.G.)

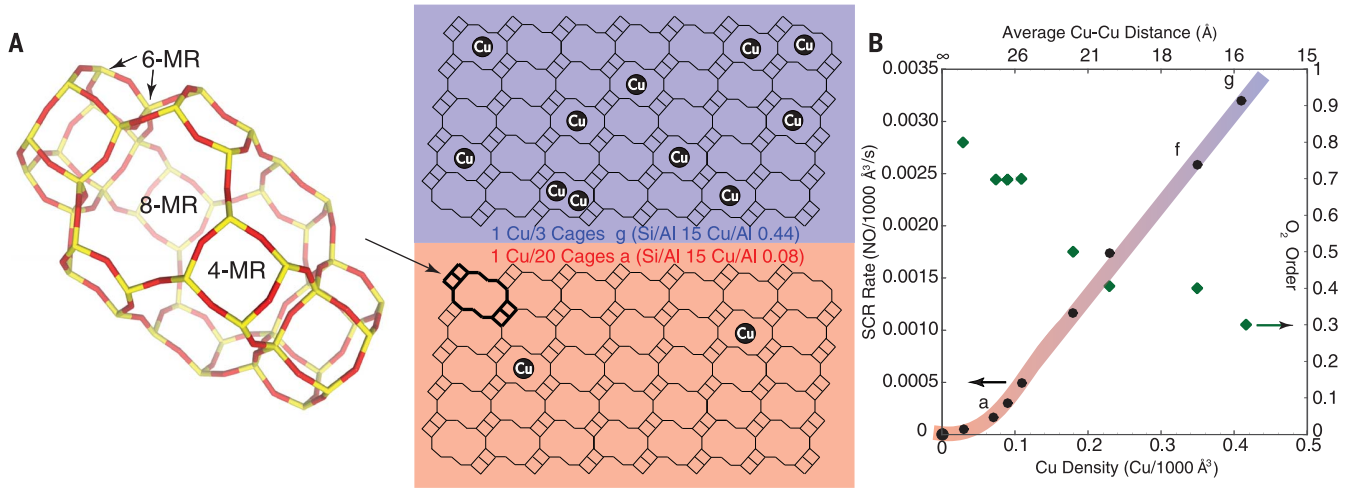

Fig. 1. Cu-density dependence of SCR rates. (**A**) The CHA cage (*36*) and schematic representation of the Cu ion densities per CHA cage in samples a and g. (**B**) Standard NO_x SCR rates (per volume catalyst; 473 K; measured in a differential reactor by using a gas mixture representative of practical low-temperature application, including 2.5% H_2O; details in SM section S2) and apparent O_2 orders measured on Cu-CHA-X samples (Si/Al = 15, table S3) of increasing Cu ion density. Colored line is a visual guide; regression fits to the quadratic (R^2 = 0.99) and linear (R^2 = 0.99) kinetic regimes are detailed in SM section S2.

conditions and temperature. The XANES data show that Cu^I is the minority oxidation state at the highest Cu density and smallest mean Cu-Cu separations (<~15 Å) during steady-state catalytic operation but that its proportion increases with decreasing Cu density to the point that it becomes the majority oxidation state in the most dilute sample (mean Cu-Cu distance ~29 Å). In this dilute limit, the operando XANES and extended x-ray absorption fine structure (EXAFS) spectra become indistinguishable from those of a Cu^I-CHA sample reduced in situ or of $Cu^I(NH_3)_2$ in aqueous solution (fig. S5 and table S4) (*10*). This observation suggests that $Cu^I \rightarrow Cu^{II}$ oxidation rates increase with Cu ion density and implies non–single site behavior in the oxidation half-cycle, a process that is not well understood mechanistically beyond the observation that it consumes O_2 (*12*).

The coordination states of site-isolated Cu^I and Cu^{II} ions under standard SCR conditions at 473 K have been explored previously in detail (*10*). X-ray absorption spectroscopy (*10*), x-ray emission spectroscopy (*19*, *20*), and density functional theory (DFT)–based models (*10*) (including ab initio thermodynamic phase diagrams in figs. S17 and S18) show that NH_3 outcompetes other gases present under standard SCR conditions, including H_2O, for binding at both Cu^I and Cu^{II} ions, which are respectively two- and four-fold coordinated. Consistent with these findings, the standard SCR reaction rate is zero order with respect to water pressure (1 to 10% atm; fig. S19). Schematic illustrations of the most probable coordination states of Cu^I and Cu^{II} ions under these conditions are shown in the inset of Fig. 2.

In the high–Cu density samples (Fig. 2, samples c to g), the first-shell Cu coordination number (CN) derived from operando EXAFS is three, consistent with the expectation for a nearly equimolar mixture of Cu^I and Cu^{II} [(*10*), table S4]. The CN decreases to two in the fully reduced (Fig. 2, samples a to b), lowest–Cu density samples, consistent with site-isolated $Cu^I(NH_3)_2$ as the most abundant reactive intermediate present during steady-state standard SCR. In this limit, the SCR turnover rate is solely limited by the $Cu^I \rightarrow Cu^{II}$ half-reaction. The increase in apparent O_2 reaction order from 0.3 to 0.8 with decreasing Cu density reinforces the increasing kinetic relevance of the $Cu^I \rightarrow Cu^{II}$ half-cycle as Cu becomes more dilute (Fig. 1). This change also corresponds with the transition from a first-order to a second-order dependence of SCR rate on Cu-ion density [Fig. 1, (*18*)]. From these observations, we conclude that the kinetically relevant O_2-consuming step in the oxidation half-cycle is sensitive to Cu density.

Cu^I site density requirements differ for oxidation with O_2 and NO_2

To probe the coupled roles of O_2 and Cu density in the oxidation half-cycle, Cu-CHA-29, Cu-CHA-20, and Cu-CHA-15 (Fig. 2, labels a, c, and h, respectively) were first reduced to the Cu^I state in flowing NO and NH_3 (details in SM section S3, figs. S6 to S8) (*10*). Then, samples were held under flowing O_2, and the transient evolution of the Cu oxidation state was monitored by using XANES. The Cu^I fraction decayed

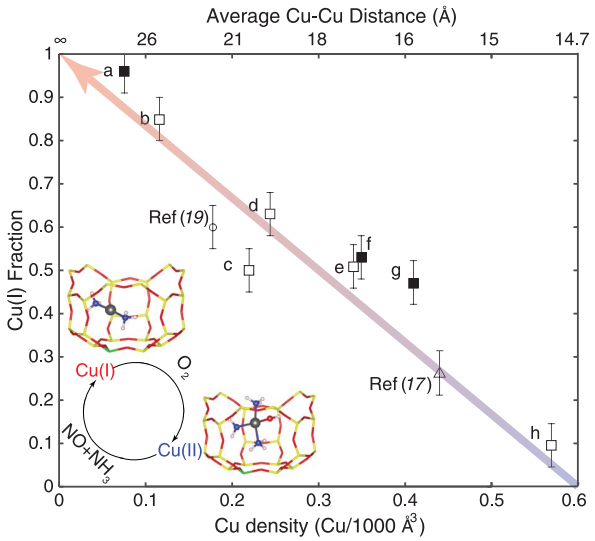

Fig. 2. Cu-density dependence of operando Cu oxidation state. The dependence of Cu^I fraction on Cu ion volumetric density during steady-state standard SCR at 473 K was measured by XANES (details in SM section S3). Data points include samples a, f, and g shown in Fig. 1 (Si/Al = 15, filled squares), samples at Si/Al = 4.5 and Si/Al = 25 (open squares), and comparable literature data [open circle Ref (*19*), Si/Al = 16; open triangle Ref (*17*), Si/Al = 4.5]. Inset shows NH_3-solvated, isolated Cu^I and Cu^{II} species previously observed and computed (*10*) to be present during standard SCR at 473 K. Gray, Cu; green, Al; yellow, Si; red, O; blue, N; and white, H. The colored arrow is a visual guide; error bars represent the absolute 5% uncertainty from linear combination XANES fitting (details in SM section S3).

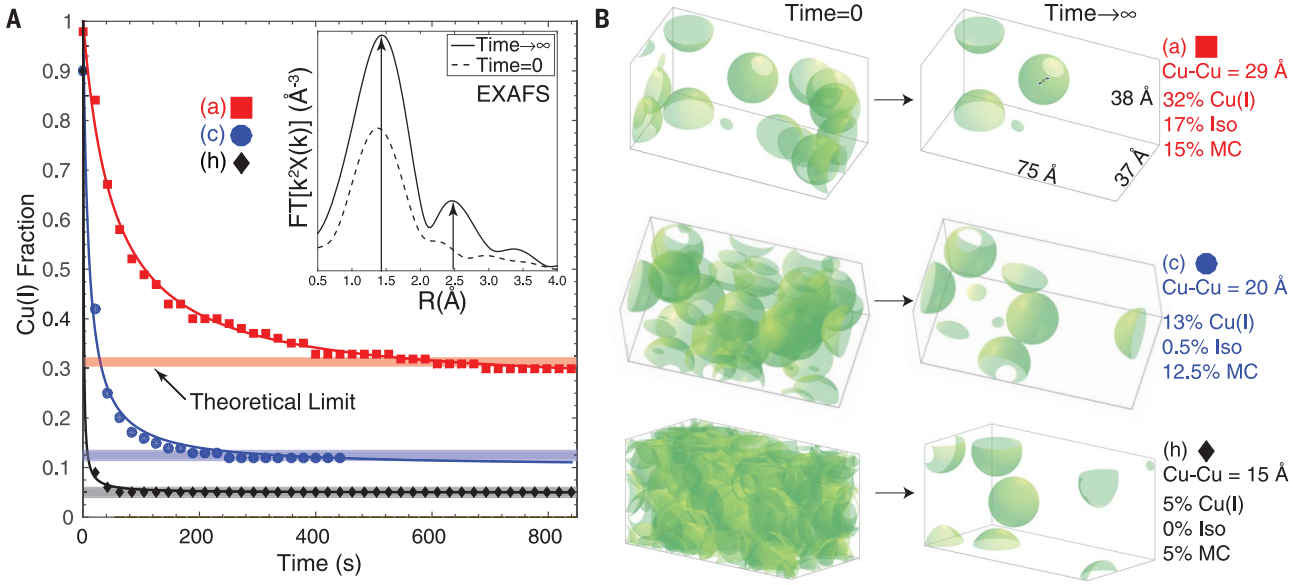

Fig. 3. Kinetics of Cu^I oxidation by O_2. (**A**) Temporal evolution of the XANES-measured Cu^I fraction is plotted for the Cu-CHA-29 (a, red), Cu-CHA-20 (c, blue), and Cu-CHA-15 (h, black) samples during transient oxidation in 10% O_2 at 473 K. Least-squares fit to Eq. 2 is shown by solid lines, and predicted recalcitrant Cu^I fractions are shown as horizontal bars. $[Cu^I]_\infty$ was set by forcing the fit through the last (longest time) data point; $[Cu^I](0)/[Cu^I]_0$ was set to 1 (full details in SM section S4). The Cu^I fractions reported contain an absolute 5% error from linear combination XANES fits (details in SM section S3). Inset, the Fourier transform of the k^2-weighted EXAFS signal (FT[$k^2\chi(k)$]) in R-space (R) of Cu-CHA-15 collected before O_2 exposure and after the transient experiment. (**B**) Snapshots taken from simulated initial (time = 0) and final (time→∞) Cu^I spatial distributions corresponding to the three samples (a, c, and h) in (A). Cu^I volumetric footprints are denoted by 9 Å–radius green spheres. Simulation results include decomposition of unoxidized Cu^I fraction into physically isolated (Iso) and functionally isolated (MC) components.

in the presence of O_2 at different rates on the three samples (Fig. 3A), and different fractions of Cu^I (0.05 to 0.30) persisted at steady state (table S6).

The dependence of the transient oxidation state response on Cu density suggests some underlying spatial requirements for $Cu^I(NH_3)_2$ ions to react with O_2. After exploring various rate laws, we found that an expression that is second order in total Cu^I density $[Cu^I]$ and offset by a recalcitrant fraction of Cu^I, $[Cu^I]_\infty$, fits the data most satisfactorily [coefficient of determination (R^2) = 0.99 (a), 0.98 (c), and 0.99 (h), Fig. 2; details in SM section S4]. Normalizing to the initial Cu^I density, $[Cu^I]_0$, the integrated rate law becomes

$$Cu^I\,\text{fraction} = \frac{[Cu^I](t)}{[Cu^I]_0} = \frac{1-[Cu^I]_\infty/[Cu^I]_0}{1+2k\left([Cu^I]_0-[Cu^I]_\infty\right)t} + \frac{[Cu^I]_\infty}{[Cu^I]_0} \quad (2)$$

where t is time and k is a pseudohomogeneous second-order rate constant for disappearance of Cu^I. Solid lines in Fig. 3A denote best-fit regressions of the data to Eq. 2. Fitted k values of (1.0, 1.7, and 8.2) × 10^{-4} m^3 mol Cu^{-1} s^{-1} for Cu-CHA-29, Cu-CHA-20 and Cu-CHA-15, respectively, increased systematically with Cu density. The variation in k demonstrates that all the reaction sites are not kinetically equivalent. Further analysis below suggests that the oxidation kinetics cannot be faithfully captured by a mean-field model.

This second-order Cu dependence suggests a pseudobimolecular reaction between two $Cu^I(NH_3)_2$ ions and O_2 during the transient experiment

$$2\left[Cu^I(NH_3)_2\right] + O_2 \rightarrow \left[(NH_3)_2Cu^{II}\text{–}O_2\text{–}Cu^{II}(NH_3)_2\right] \quad (3)$$

Oxygen-bridged Cu dimers are well known in Cu-zeolite chemistry (*21*–*23*) and find analogies in the biological chemistry of Cu that prevails at lower temperatures (*24*–*29*). These dimers can adopt various oxygen-bridging configurations (*25*, *30*). To probe the plausibility of this reaction between two caged $Cu^I(NH_3)_2$ centers, we turned to DFT (computational details in SM section S5).

We first considered the energy landscape for two $Cu^I(NH_3)_2$ ions to occupy the same CHA cage. Starting from two $Cu^I(NH_3)_2$ ions in adjacent cages that share an Al T-site vertex (Fig. 4, structure A), the computed barrier for one $Cu^I(NH_3)_2$ to diffuse through an 8-MR window into the adjacent $Cu^I(NH_3)_2$-containing cage (structure B) is 35 kJ mol^{-1}, consistent with prior estimates of $Cu^I(NH_3)_2$ diffusion barriers into an empty cage (*10*, *31*). The net pairing cost is 23 kJ mol^{-1}. Thus, transport between adjacent Al-sharing cages is expected to be facile at temperatures of catalytic interest. Two $Cu^I(NH_3)_2$ ions bind O_2 more effectively (−59 kJ mol^{-1}) than does an isolated $Cu^I(NH_3)_2$ (−26 kJ mol^{-1}) (table S10 and fig. S14), and the O_2 binding energy more than offsets the energy cost for two $Cu^I(NH_3)_2$ to cohabit the same cage. Initial reaction likely generates the end-on spin-triplet species shown in Fig. 4 (structure C), and further rearrangement and dissociation of O_2 across two Cu^I centers ultimately leads to the di-oxo structure E, containing two four-fold-coordinated Cu^{II} centers. Conversion of structure C into D is spin forbidden; the effective barrier in similar ligand environments is estimated to be 20 kJ mol^{-1} (*24*). Subsequent conversion of structure D into E occurs with a modest barrier. The rate-limiting process across this entire cascade (A to E, table S9) is the migration of Cu^I through the 8-MR; beyond that point, reaction energies are computed to be independent of the zeolite cage. Thus, the primary role of the zeolite support in this oxidation process is to regulate Cu^I mobility.

Structure E is consistent both with XANES-observed Cu^{II} oxidation state and with the first- and second-shell features extracted from EXAFS (Fig. 3A, inset, and figs. S9 to S11) at the end of the transient O_2 oxidation experiment. Thus, experiment and computation both reveal a second Cu^{II} state of the catalyst, distinct from framework-bound Cu^{II} observed after oxidative treatments and from NH_3-solvated Cu^{II} detected during low-temperature standard SCR (*10*, *20*). Exposure of samples to NO and NH_3 at 473 K after the transient O_2 oxidation experiments reduces all sites to the original mononuclear Cu^I state, demonstrating that the SCR redox cycle can be closed through sequential stoichiometric reactions

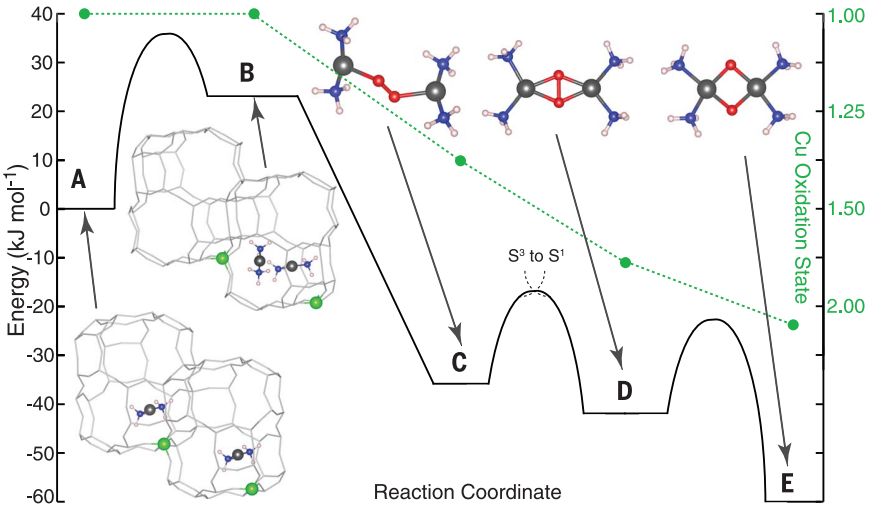

Fig. 4. Simulation of O_2 adsorption and oxidation of two $Cu^I(NH_3)_2$ equivalents. DFT-computed energy landscape is shown for the diffusion of $Cu^I(NH_3)_2$ through an 8-MR CHA window into an adjacent cage and subsequent bimolecular reaction with O_2. All minima and transition states were computed here, except C to D, which is taken from (*24*). Gray, Cu; green, Al; red, O; blue, N; and white, H.

(SM section S6, fig. S12). Further, subsequent O_2 treatment recovers the same transient response and the same fraction of Cu^I sites that are unresponsive to O_2 exposure (table S7), indicating that Cu^I ions do not irreversibly aggregate during O_2 exposure, but return to their original site-isolated state after each reduction step.

To verify that the residual Cu^I fraction did not represent a physically inaccessible or chemically distinct site, transient O_2 experiments were compared with an analogous transient NO_2 experiment (details in SM section S3) on reduced forms of the same three samples (figs. S6 to S8). After NO_2 exposure at 473 K, the Cu^I fraction decayed with time as in the O_2 experiment, but the Cu^I absorption edges disappeared completely after ~300 s. Further, the decrease in Cu^I fraction with time is best described [R^2 = 0.98 (a), 0.98 (c), and 0.89 (h); details in SM section S4] by a pseudo–first order rate expression with apparent rate constants (0.030 s^{-1}) that are independent of Cu density (SM section S4, fig. S13). Thus, all Cu^I sites are equivalently susceptible to oxidation by NO_2. We compute the reaction energy for NO_2 binding to $Cu^I(NH_3)_2$ to be −46 kJ mol^{-1} and to generate a Cu^{II} center (SM section S5, fig. S14, and table S10).

We conclude that the spatial proximity of isolated Cu^I ions, and not the presence of minority dimeric Cu species at low Cu densities, is responsible for the transition in the standard SCR turnover rate from a quadratic to linear dependence on Cu ion density with increasing Cu density (Fig. 1B). The steady-state and transient experiments and DFT models are consistent with a $Cu^I \rightarrow Cu^{II}$ half-cycle that combines two $Cu^I(NH_3)_2$ complexes with one O_2 molecule to create a previously unobserved binuclear Cu^{II} intermediate (Eq. 3 and Fig. 4).

The available data exclude the possibility that O_2 activation occurs on a persistent minority fraction of Cu ion pairs within single zeolite cages (*32*). First, the fraction of isolated $Cu^I(NH_3)_2$ complexes that could be reversibly oxidized with O_2 (Fig. 3A) exceeds by 10-fold the fraction of Cu pairs within a single cage if Cu were randomly dispersed on the zeolite support (SM section S7, fig. S15). Second, steady-state and transient rates of Cu^I oxidation with O_2 would exhibit a first-order dependence on Cu density, as observed with NO_2 as the oxidant. Rather, these results imply a pseudohomogeneous reaction between equivalent site-isolated Cu^I ions with mobilities constrained in a manner that limits the total fraction of sites reactive toward O_2.

Solvation by ammonia confers mobility to single Cu ions

To assess the mobility of $Cu^I(NH_3)_2$ complexes over time scales inaccessible to conventional ab initio molecular dynamics, we turned to ab initio metadynamics (SM section S8), taking Cu-Al coordination distance as the collective variable, using a supercell with a minimum image distance of >10 Å (SM section S8), and sampling at 473 K. Free energy was minimized at a Cu-Al distance of 4.7 Å and increased with Cu-Al separation until the Cu ion entered an 8-MR window separating two cages, at 8 Å (Fig. 5). Free energy decreased as the Cu ion moved into the adjacent cage, before increasing again as the Cu-Al distance exceeded 9 Å. Comparison with a point-charge model indicates that electrostatics dominate this distance-dependent free energy (SM section S9, Fig. 5). From the computed free-energy landscape, we estimate the hopping rate for a $Cu^I(NH_3)_2$ to leave its resting cage to be 6×10^6 s^{-1} at 473 K, much faster than steady-state SCR turnover rates (table S3), and the equilibrium fraction of Cu ions outside their resting cage to be 1.4×10^{-5} at 473 K.

$Cu^I(NH_3)_2$ migration is thus rapid at 473 K but constrained by electrostatic tethering to charge-compensating framework Al sites. We next used this concept to predict the unoxidized fraction of $Cu^I(NH_3)_2$ in the transient O_2 experiments (Fig. 3A), assuming that Cu ions are randomly associated with Al in the CHA lattice, that each Cu can access a limited diffusion volume, and that only Cu^I ions with overlapping diffusion volumes can form an O_2-bridged Cu pair (Fig. 4). To exercise the model, we distributed Al onto a periodic supercell of the CHA lattice following Löwenstein's rule (*33*), occupied sites with Cu following previously validated rules (*10*), counted the number of overlapping diffusion spheres at a given radius (Fig. 3B, t = 0) permitting each Cu to be counted only once, and repeated until the average unoxidized Cu^I fraction converged (SM section S10 and fig. S16). At the end of a single simulation, the unoxidized Cu^I fraction consisted of Cu ions that either were initially physically isolated from all other Cu (Iso) or were functionally isolated because they shared overlapping diffusion volumes with Cu ions that had more than one potential partner, the losers in a molecular game of musical chairs (MC). Representative initial and final simulation snapshots are shown in Fig. 3B for Cu densities corresponding to Cu-CHA-15, Cu-CHA-20, and Cu-CHA-29, and the predicted fraction of unoxidized Cu^I assuming a diffusion radius of 9 Å are plotted as solid horizontal bars in Fig. 3A. Model results agree quantitatively with both experimental observation and the metadynamics observation of a ~9 Å maximum diffusion distance, implying that the Cu sites are neither conventionally heterogeneous (immobile) nor homogeneous (mobility governed by molecular diffusion) and demonstrating that the fraction of spectator $[Cu^I]_\infty$ sites is a consequence of regulated and localized mobility due to electrostatic tethering.

These observations resolve the outstanding issues regarding SCR catalysis raised in the introduction. NH_3 solvates and mobilizes discrete Cu active sites under low-temperature SCR conditions. When the activation of O_2 is not rate controlling, NH_3-solvated Cu ions appear catalytically equivalent, such that rates increase linearly with their number density. In this regime, the zeolite framework itself has only a weak influence on the SCR turnover rate (*10*) because it functions primarily as an ionic host for homogeneous-like NH_3-ligated Cu^{II} complexes. Experiments performed on samples with low Cu density revealed, however, that a homogeneous picture of the SCR mechanism is incomplete.

Simulations reveal that NH_3-solvated Cu^I ions have sufficient mobility to travel through 8-MR CHA windows, visit adjacent cages, and form Cu site pairs that activate O_2 via Eq. 3. Because of this requirement for dynamic Cu pairing, SCR rates scale approximately second order with Cu density under conditions in which the $Cu^I \rightarrow Cu^{II}$ oxidation by O_2 is rate determining, consistent

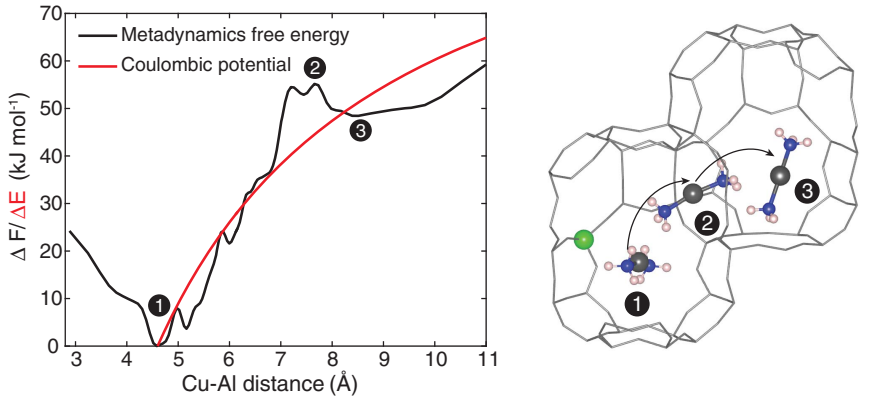

Fig. 5. Simulated $Cu^{I}(NH_3)_2$ diffusion up to 11 Å from charge-compensating Al. On left, the metadynamics-computed free energy at 473 K of $Cu^{I}(NH_3)_2$ in the 72–T site CHA supercell versus Cu-Al distance. The red line is the energy profile predicted from a point-charge electrostatic model, described in SM section S9. Labeled are reactant state (1) [$Cu^{I}(NH_3)_2$ in the same cage as Al], transition state (2) [$Cu^{I}(NH_3)_2$ diffusion through 8-MR], and product state (3) [$Cu^{I}(NH_3)_2$ in the neighboring cage without Al]. Corresponding representative $Cu^{I}(NH_3)_2$ configurations from the trajectories are shown on the right. Gray, Cu; green, Al; blue, N; and white, H.

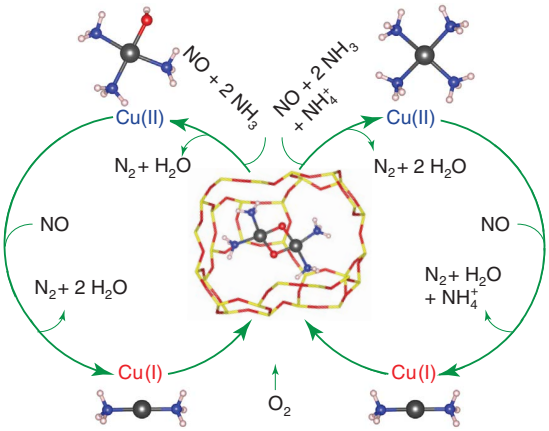

Fig. 6. Proposed low-temperature SCR catalytic cycle. Reduction steps proceed on site-isolated Cu^{II} ions residing near one (left-hand cycle) or two (right-hand cycle) framework Al centers with constrained diffusion of Cu^{I} ions into single cages and oxidation by O_2 (inner step). NH_4^+ is formed and consumed in the right-hand cycle to maintain stoichiometry and charge balance. Gray, Cu; yellow, Si; red, O; blue, N; and white, H.

with quantitative analysis of the transient oxidation of Cu^{I} with O_2. In contrast with previous assertions (*34*), binuclear Cu^{II} intermediates can be detected experimentally and are structurally distinct from the mononuclear NH_3-solvated Cu^{II} observed in operando (*10*, *20*), and the number of such binuclear sites that can form on a given Cu-CHA sample can be quantitatively predicted. These results motivate a revision of previous mechanisms to incorporate this dynamic coupling of isolated Cu ions, as illustrated in Fig. 6. Isolated, NH_3-solvated Cu^{II} ions charge-compensating either one (left cycle) or two (right cycle) framework Al sites are reduced by NO and NH_3 to produce N_2, H_2O, and $Cu^{I}(NH_3)_2$. These two paths are distinguished only by the fate of the proton that is also generated (*10*). Mobile $Cu^{I}(NH_3)_2$ species can diffuse and combine in a reaction that consumes O_2 and generates the Cu^{II} dimer intermediate observed here. We confirmed that this binuclear Cu^{II} complex reacts with two equivalents of NO per Cu (SM section S6, fig. S12) to regenerate $Cu^{I}(NH_3)_2$ and close the SCR cycle.

A key aspect of our model is that Cu ions supported on the zeolite are neither mobile as prescribed by molecular diffusion processes, as in a homogeneous catalyst, nor segregated into separate ensembles of active and inactive sites, as in a heterogeneous catalyst. Rather, all Cu ions located within diffusion distances of other ions can potentially form Cu pairs dynamically and reversibly during the SCR cycle, at rates influenced by the mobility and effective diffusion distances of Cu ions. Thus, rates of O_2-assisted oxidations are sensitive to Cu proximity and could also be sensitive to the zeolite support composition and topology. By contrast, all NH_3-solvated Cu^{I} sites are equivalently susceptible to first-order oxidation by NO_2, independent of Cu spatial density, and are subsequently reducible by NO and NH_3. These observations demonstrate that fast SCR, in which oxidation capacity is provided by NO_2 rather than O_2

$$2NH_3 + NO + NO_2 \rightarrow 2N_2 + 3H_2O \qquad (4)$$

is not linked through a common intermediate to standard SCR under conditions in which Cu sites are solvated by NH_3 (*16*). NO_2 oxidants accelerate SCR rates both by accelerating Cu^{I} oxidation kinetics and by engaging a larger fraction of Cu sites in the catalyst.

At higher temperatures (>523 K), standard SCR rates are independent of Cu density (*12*, *18*), the apparent activation energy increases to 140 kJ mol^{-1} (*18*), and Cu ions lose their NH_3 solvation shell (*12*), implicating the involvement of different O_2 activation steps that do not occur at the Cu ion pairs formed dynamically at lower temperatures (<523 K). Of greater practical importance to NO_x emissions control is to increase SCR rates at even lower temperatures (<473 K) (*12*). The results here imply that standard SCR onset ("light-off") temperatures, which are observed to depend on zeolite composition, topology, and Cu distribution (*35*), are sensitive to changes in rate-determining O_2 activation steps. Thus, optimization of Cu spatial distribution and promotion of Cu mobility are promising strategies for accelerating Cu^{I} oxidation rates and improving low-temperature SCR catalysts.

Outlook

Our results point to a previously unrecognized catalytic mechanism that embodies salient features of homogeneous and heterogeneous catalysts. This mechanism encompasses solvent mobilization of discrete active site precursors (e.g., single metal ions) and ionic bonds to the support that limit their mobility. The active site precursor has an effective diffusion distance and occupies a volumetric footprint that restricts its interactions only to other precursors within overlapping volumes; such catalytic behavior cannot be described by mean-field, Langmuir kinetics. The ionic tethering motif provides opportunities to confer catalytic benefits beyond immobilization strategies based on covalent anchors or tethers. This motif enables the in situ dynamic generation of multinuclear complexes implicated as active sites in O_2 activation and therefore could also apply to other reactions, such as the partial oxidation of methane to methanol on Cu-zeolites. We expect that design parameters to regulate the mobility of active sites and their precursors would include the structure, composition and electronic conductivity of the support, and the molecules that solvate such sites to promote their mobility. Manipulating these variables could open approaches to catalyst design for a wide variety of reactions by combining knowledge from homogeneous and heterogeneous catalysis.

REFERENCES AND NOTES

1. J. M. Thomas, *Proc. R. Soc. A* **468**, 1884–1903 (2012).
2. M. Boudart, *Chem. Rev.* **95**, 661–666 (1995).
3. K. Ding *et al.*, *Science* **350**, 189–192 (2015).
4. J. Jones *et al.*, *Science* **353**, 150–154 (2016).

5. E. J. Peterson *et al*., . *Nat. Commun.* **5**, 4885 (2014).
6. G. Kyriakou *et al*., *Science* **335**, 1209–1212 (2012).
7. H. Wei *et al*., *Nat. Commun.* **5**, 5634 (2014).
8. M. Yang *et al*., *Science* **346**, 1498–1501 (2014).
9. M. Yang *et al*., *J. Am. Chem. Soc.* **137**, 3470–3473 (2015).
10. C. Paolucci *et al*., *J. Am. Chem. Soc.* **138**, 6028–6048 (2016).
11. J. M. Thomas, R. Raja, D. W. Lewis, *Angew. Chem. Int. Ed.* **44**, 6456–6482 (2005).
12. C. Paolucci, J. Di Iorio, F. Ribeiro, R. Gounder, W. Schneider, in *Advances in Catalysis*, C. Song, Ed. (Elsevier, 2016), vol. 59, pp. 1–107.
13. S. T. Korhonen, D. W. Fickel, R. F. Lobo, B. M. Weckhuysen, A. M. Beale, *Chem. Commun. (Camb.)* **47**, 800–802 (2011).
14. E. Borfecchia *et al*., *Chem. Sci. (Camb.)* **6**, 548–563 (2015).
15. C. Paolucci *et al*., *Angew. Chem. Int. Ed.* **53**, 11828–11833 (2014).
16. T. V. W. Janssens *et al*., *ACS Catal.* **5**, 2832–2845 (2015).
17. S. A. Bates *et al*., *J. Catal.* **312**, 87–97 (2014).
18. F. Gao *et al*., *J. Catal.* **319**, 1–14 (2014).
19. T. Günter *et al*., *Chem. Commun. (Camb.)* **51**, 9227–9230 (2015).
20. K. A. Lomachenko *et al*., *J. Am. Chem. Soc.* **138**, 12025–12028 (2016).
21. P. J. Smeets *et al*., *J. Am. Chem. Soc.* **132**, 14736–14738 (2010).
22. P. Vanelderen *et al*., *J. Am. Chem. Soc.* **137**, 6383–6392 (2015).
23. J. S. Woertink *et al*., *Proc. Natl. Acad. Sci. U.S.A.* **106**, 18908–18913 (2009).
24. M. Metz, E. I. Solomon, *J. Am. Chem. Soc.* **123**, 4938–4950 (2001).
25. L. M. Mirica, X. Ottenwaelder, T. D. P. Stack, *Chem. Rev.* **104**, 1013–1045 (2004).
26. L. M. Mirica *et al*., *Science* **308**, 1890–1892 (2005).
27. P. Chen, E. I. Solomon, *Proc. Natl. Acad. Sci. U.S.A.* **101**, 13105–13110 (2004).
28. S. D. McCann, S. S. Stahl, *Acc. Chem. Res.* **48**, 1756–1766 (2015).
29. B. R. Goodman, K. C. Hass, W. F. Schneider, J. B. Adams, *J. Phys. Chem. B* **103**, 10452–10460 (1999).
30. E. I. Solomon *et al*., *Chem. Rev.* **114**, 3659–3853 (2014).
31. L. Chen, J. Jansson, M. Skoglundh, H. Grönbeck, *J. Phys. Chem. C* **120**, 29182–29189 (2016).
32. H. Falsig, P. N. R. Vennestrøm, P. G. Moses, T. V. W. Janssens, *Top. Catal.* **59**, 861–865 (2016).
33. W. Lowenstein, *Am. Mineral.* **39**, 92–96 (1954).
34. F. Gao, D. Mei, Y. Wang, J. Szanyi, C. H. F. Peden, *J. Am. Chem. Soc.* **139**, 4935–4942 (2017).
35. J. H. Kwak, R. G. Tonkyn, D. H. Kim, J. Szanyi, C. H. F. Peden, *J. Catal.* **275**, 187–190 (2010).
36. C. Baerlocher, L. B. McCusker, Database of zeolite structures (2017); www.iza-structure.org/databases/.

ACKNOWLEDGMENTS

Full details of experiments and computational models are provided in the supplementary materials. Financial support was provided by the National Science Foundation GOALI program under award numbers 1258715-CBET (Purdue) and 1258690-CBET (Notre Dame), the National Science Foundation Faculty Early Career Development Program under award number 1552517-CBET (R.G.), Cummins, Inc. (I.K., A.J.S., A.A.P., J.D.A.-C.). and The Patrick and Jane Eilers Graduate Student Fellowship for Energy Related Research (C.P.). Use of the Advanced Photon Source is supported by the U.S. Department of Energy, Office of Science, and Office of Basic Energy Sciences, under Contract No. DE-AC02-06CH11357. We thank the Center for Research Computing at Notre Dame, and EMSL, a DOE Office of Science User Facility sponsored by the Office of Biological and Environmental Research and located at Pacific Northwest National Laboratory, for computational resources.

SUPPLEMENTARY MATERIALS

www.sciencemag.org/content/357/6354/898/suppl/DC1
Materials and Methods
Figs. S1 to S20
Tables S1 to S11
References (*37*–*68*)
Database S1

2 May 2017; accepted 7 July 2017
Published online 17 August 2017
10.1126/science.aan5630